Electrochemical wall shear rate microscopy of collapsing bubbles

Fabian Reuter[*] and Robert Mettin

Christian Doppler Laboratory for Cavitation and Micro-Erosion, Drittes Physikalisches Institut,
Georg-August-Universität Göttingen, Friedrich-Hund-Platz 1, 37077 Göttingen, Germany

An electrochemical high-speed wall shear raster microscope is presented. It involves chronoamperometric measurements on a microelectrode that is flush-mounted in a submerged test specimen. Wall shear rates are derived from the measured microelectrode signal by numerically solving a convection-diffusion equation with an optimization approach. This way, the unsteady wall shear rates from the collapse of a laser pulse seeded cavitation bubble close to a substrate are measured. By planar scanning, they are resolved in high spatial resolution. The wall shear rates are related to the bubble dynamics via synchronized high-speed imaging of the bubble shape.

I. INTRODUCTION

Cavitation bubbles nucleate in liquids under strong tensile stress in fast flows or acoustic fields. These vapor- or gas-filled cavities typically form larger groups and show complex behavior driven by oscillation, translation, and mutual interaction. The dynamics of individual bubbles include volume expansion, collapse and rebound, deformations, and splitting and coalescence with adjacent bubbles [1–3]. Due to their nonlinear oscillation behavior, the bubbles introduce a multitude of effects throughout the liquid. One aspect of great practical relevance is the generation of intense microconvection from shear flows, exploited for instance in mixing or cleaning applications. For its systematic investigation, it is reasonable to separate effects and consider single bubbles.

In the idealized case, one single, spherical bubble, however, freely oscillating and eventually collapsing in an unbounded liquid, can only assume (spherically) symmetric shapes and can therefore only produce flow fields of the same symmetry. But if the bubble dynamics is restricted by a solid surface nearby, it changes dramatically. Then, the collapse of a single bubble is generally accompanied by the formation of a liquid jet. It pierces the bubble and, in the case of a rigid boundary, impacts on the substrate (see Refs. [4–10]). This is potentially a violent process as kinetic energy is concentrated to a small liquid volume. As the bubble is pierced by the jet it takes a toroidal shape and shows characteristic toroidal bubble dynamics which once more concentrate kinetic energy to small liquid volumes [5,7,9,11–18]. Additionally, during collapse, the bubble translates through the liquid, often towards the substrate so that the subsequent dynamics proceed directly at the substrate [12,19].

All these aspects of bubble dynamics are involved in the generation of intense convection with large gradients, specifically directly at solid boundaries. Thus, a cavitation bubble is a generator of high wall shear rates which play a role in cavitation erosion and are crucial in applications such as ultrasonic or hydrodynamic cleaning [18,20–22]. Furthermore, this feature of cavitation bubbles is exploited in biological and medical contexts [23,24], for example, to reversibly or irreversibly alter membrane properties by mechanical means of cavitation, to permeabilize membranes for cell disruption or drug delivery, and potentially also gene transfer into cells [12,25–31].

---

[*]Corresponding author: freuter@mailbox.org

Even though flow-induced alterations of surfaces are largely determined by the time evolution of pressures and shear stresses imposed on them, experimental tools are mainly lacking for the investigation of cavitation-induced shear rates in the immediate vicinity of a boundary. This follows from the fact that the experimental investigation and measurement of bubble generated wall shear rates is challenging for a number of reasons. First of all, the bubble dynamics is very fast. The life time of the submillimeter bubbles under consideration here is only about $100\,\mu$s, the involved flows may persist even shorter. At the same time, flow phenomena are very local. The bubble radius may expand to several $100\,\mu$m, while the spatial scale of the flow patterns extends to only a fraction of that. Thus, flow fields with extreme variations, spatial and temporal ones, are produced. Therefore, the applicability of many standard flow and wall shear rate measurement methods is limited. Consequently, the dynamic wall shear rates generated by collapsing cavitation bubbles are largely unknown.

Employing hot-wire anemometry, Dijkink and Ohl [61] detected a peak value of the wall shear rate above $10^6\,\mathrm{s}^{-1}$, which already indicates the order of magnitude to be expected. Here we aim at a spatiotemporal resolution of the wall shear rates to gain a more complete picture. For this purpose, an electrochemical setup to measure wall shear rates is presented. As wall shear sensor, a microelectrode is embedded into a substrate operated in a chronoamperometric measurement configuration. The chronoamperometric technique used here is based on a simple principle. An electrode is submerged in an electrolyte solution and held at an electric potential for a defined (redox) reaction of the electrolyte to occur. The reaction current is measured over time ("the chronoamperometric signal"). The redox reaction at the electrode results in a zone in the solution where the electrolyte concentration depletes so that the current decreases. With appropriate experimental conditions, the current is only limited by the transfer rate of the electrolyte to the depletion zone which is determined by diffusion and convection [32]. The usage of this measurement principle for flow measurements is a well-established technique for the analysis of *steady* flows, often performed with macroelectrodes [33–35]. Analytical expressions relating limiting currents to flow velocities or wall shear rates have been deduced for various geometries in the equilibrium under steady flow conditions [36,37]. However, the transient currents produced by unsteady flow fields are much less explored.

Electrochemical methods in general (voltammetric or amperometric ones) were applied in complex cavitation environments by various authors. Consistently a substantial increase of mass transfer to substrate surfaces was proved due to bubble activity [38–47]. However, information about the absolute velocities and shear rates generated from cavitation at electrode surfaces stayed incomplete. In addition, so far only little work on single bubbles has been published [48,49], even though collapsing bubbles are the principal cause for the generation of wall shear and for the mass transfer enhancement by ultrasound.

The electrochemical wall shear rate microscope presented here employs a chronoamperometric measurement setup and allows for the measurement of the wall shear rates in high spatial and temporal resolution through hydrodynamically induced electrochemical perturbations. To this end, a one-dimensional model coupling convection and diffusion is developed. The wall shear rate microscope is operated to sample the wall shear rates produced by the collapse of a single collapsing microbubble. The wall shear rates are related to the bubble dynamics via synchronous high-speed imaging of the bubble shape evolution.

II. EXPERIMENTAL SETUP AND METHODS

The experimental setup consists of two parts: the arrangement for the production and imaging of single bubbles (Sec. II A), and the electrochemical wall shear raster microscope (Sec. II B). For a simplified sketch of the entire setup; see Fig. 1. The electronic devices of both parts are controlled and synchronized by a LabVIEW script developed for this purpose. For synchronization and timings, three pulse generators of type Stanford RS DG 535 (providing in total 12 channels) and an oscilloscope (Tektronix DPO 4104) are employed.
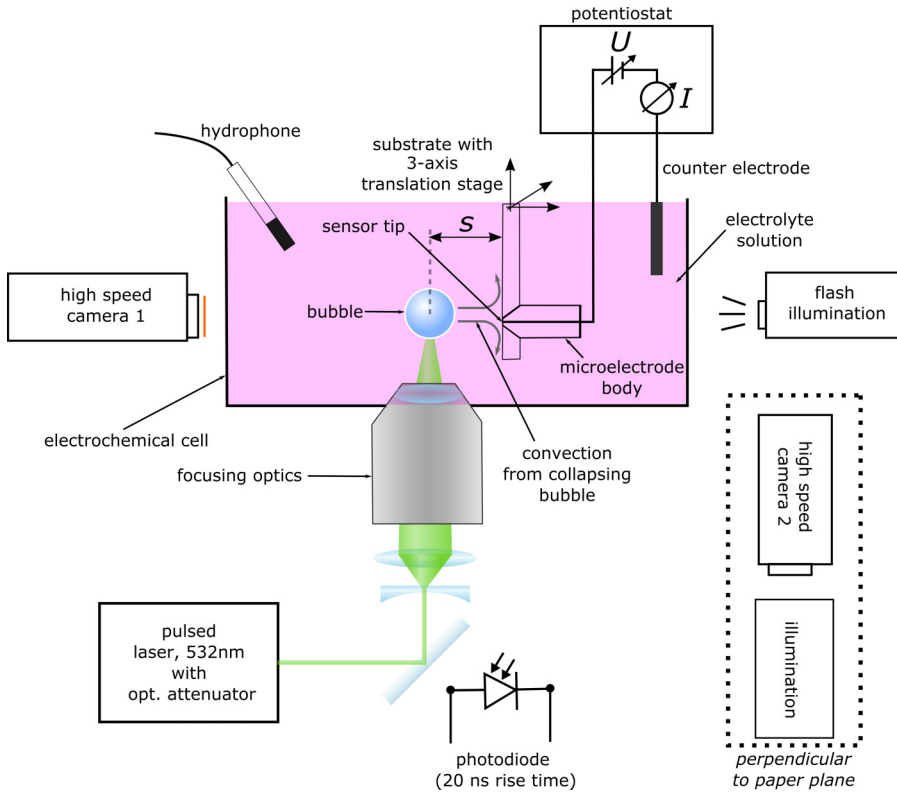
FIG. 1. Experimental setup.

A. Bubble generation and imaging

All measurements are conducted in a water-filled glass cuvette (dimensions $50 \times 50 \times 50$ mm^3). For each chronoamperometric probing, one bubble is seeded by plasma generation from a laser pulse focused in vicinity of a sample substrate for which a PMMA-slide (thickness 1 mm) with a flush mounted wall shear rate sensor is used (see Sec. II B). After each probing, the sensor is moved and a bubble with identical properties is generated at the same, precisely defined position of the laser focus. This way, an area of 1300×700 μm^2 is scanned (Cartesian grid, step width 25 μm). For noise reduction, measurements are repeated three times and shear rates are averaged. In total, for the wall shear rate plane presented here, about 4300 single measurements were made.

For plasma-induced bubble generation, a Nd:YAG laser (Litron nano S, wavelength 532 nm, pulse length about 5 ns) is used. The beam is focused by a custom-made objective of high numerical aperture and working distance (NA > 0.4, working distance 15 mm). For aberration-free focusing, the optics output aperture is submerged in solution. To our experience, the lower the energy needed to produce optical breakdown, the better the seeded bubbles in terms of sphericity and repeatability. A laser pulse energy of about 1 mJ is adjusted by optical attenuation and turned out to be sufficient for reliable production of optical breakdowns. The laser beam is focused parallel to test substrate and sensor, to avoid any spurious signal from light sensor interaction (see Reuter *et al.* [49]). Bubbles of maximum radius $R_{\mathrm{max}} = 425$ μm are produced at a normalized stand-off distance from the test substrate of $\gamma = 0.98 \cong 1$. The stand-off distance is defined by $\gamma = s/R_{\mathrm{max}}$, where s denotes the distance between bubble centre and substrate (s is sketched in Fig. 1). The normalized stand-off distance fully characterizes, over a wide range of parameters, the dynamics of a bubble that collapses at a flat boundary.

Generation and collapse of the bubble are accompanied by characteristic shock wave emissions. The resulting acoustic signature of the bubble is measured with a hydrophone (Reson TC 4038) in conjunction with an oscilloscope (Tektronix DPO 4104). This allows the determination of (I) the shock wave amplitudes and (II) the bubble life time T_L, i.e., the time from plasma generation to the first bubble collapse. Reduced shock wave amplitudes are an indicator of imperfectly shaped bubbles, therefore only bubbles with shock wave amplitudes that deviate less than 5% from the 95% quantile amplitude are included in the evaluation. The bubble life time is a measure for the maximum bubble radius: between T_L and R_{max} a linear relation holds (for a fixed γ); see Refs. [6,50]. Only bubbles with R_{max} deviating less than 5% from the average radius of 425 μm are included in the evaluation.

The bubble shape evolution is recorded by a high-speed video camera (Photron Fastcam SA5, equipped with an Infinity K2 CF-3 objective, and a filter blocking the 532 nm laser emission) at frame rates between 70,000 and 180,000 fps with exposure times of $0.37 - 1\,\mu$s. The high-speed video camera operates simultaneously to the electrochemical measurement.

For synchronization of the electrochemical measurement with the high-speed imaging, the camera exposure signal is recorded, a fast photo diode (Thorlabs DET 10A/M) is employed to register the light of the bubble seeding laser, and the auxiliary A/D-channel that is provided by the potentiostat is used. This way, synchronization with a precision better than 1 μs is achieved.

Another camera (PCO sensicam, exposure times 10 μs) is operated in a perspective perpendicular to the video camera. For illumination, two flashes are used (one photographic discharge lamp (Metz) and an in-house built pulsed LED). With this arrangement, the position of the bubble with respect to the electrode tip and the maximum bubble radius are measured, which determine the stand-off distance $\gamma = s/R_{max}$.

B. Electrochemical wall shear microscope

The main portions of the wall shear microscope are a high-speed chronoamperometric setup, a three-axis translation stage (nanometer-precision), and an algorithmic implementation of a physical model to derive wall shear rates from the chronoamperometric data. The chronoamperometric measurements are described in Sec. II B 1, the modeling in Sec II B 2.

1. Chronoamperometric measurements

The chronoamperometric measurements are performed with a potentiostat (Gamry Reference 600) operated at its maximum sampling frequency of 300 kHz (sampling period $T_S = 3.33\,\mu$s). To achieve the fastest electrical response possible, all internal electrical filters are turned off. Since no stabilizing capacitors are present in the circuit and because the measured currents are very small (in the order of 100 nA), special efforts are undertaken to minimize noise. High-voltage discharging devices such as laser, photographic flash drivers, etc. are placed remotely. Additionally, common grounding between the numerous electrical devices is installed and the measurement setup at the cuvette is shielded with aluminum foil. Furthermore, during post-processing, the current is de-noised with a wavelet filter and corrected for residual (ohmic) currents by subtraction of the current baseline.

As wall shear rate sensor, a platinum electrode of diameter $d_e = 25\,\mu$m (custom made by Sensolytics) is operated as working electrode. It is sealed in a conical glass body (tip diameter approximately 5 mm) and flush mounted into the sample substrate. As counter electrode, a platinum wire is submerged close to the working electrode. The reference electrode shares the same platinum wire.

The electrolyte solution consists of deionized water (conductivity $< 0.5\,\mu$S/cm) with a Faradaic electrolyte (ruthenium hexamine chloride salt [Ru(NH$_3$)$_6$]Cl$_3$, Sigma-Aldrich, concentration $c_0 = 0.03$ M) and a buffer electrolyte (potassium nitrate, KNO$_3$, 99.999% Sigma-Aldrich, 0.18 M). The working potential is chosen as 0.7 V based on cyclic voltammetry prior to the chronoamperometric measurements. This is the potential where the Faradaic reaction is maximum, but without any signs of secondary reactions. The following (reversible) reduction reaction takes place at the working electrode:

$$\text{Ru(NH}_3\text{)}_6^{3+} \rightarrow \text{Ru(NH}_3\text{)}_6^{2+} + \text{e}^-.$$

Under the present conditions (and after correction for residual currents), the current can be considered as purely Faradaic; i.e., it stems solely from the redox reaction. The diffusion coefficient of the ruthenium metal-complex is $D = 9.1 \times 10^{-10}\,\text{m}^2/\text{s}$ [51]. For the viscosity of the aqueous solution, the value of water at $20\,°\text{C}$ is used ($\eta = 1.00 \times 10^{-3}\,\text{Pa} \cdot \text{s}$) because the increase of η by the presence of the electrolyte is expected to stay below 5% [52]. The substrate with the flush mounted electrode is mounted on three piezo-driven precision translation stages. One axis allows for the precise adjustment of the bubble to substrate stand-off distance, the other two axes allow for a spatial scanning of wall shear rates in planes [Physik Instrumente, $2\times$ PI M-404.4DG (12 nm resolution) and $1\times$PI N-661.21A (20 nm resolution)]. The stages are computer controlled by the LabVIEW script.

2. Derivation of the wall shear rates from the chronoamperometric data

A few assumptions can greatly simplify the description of the physical processes in the diffusion layer. Under the present conditions, the Damköhler number Da ($Da = \frac{\text{time scale of flow}}{\text{time scale of chemical reaction}}$) for the redox couple is very large [53]. That means, once an electrolyte molecule is encountered at the electrode surface, its reduction reaction proceeds quasi-instantaneously. Therefore, the electrode current is determined only by the flux of the electrolyte toward the electrode. Migration, i.e., the flux resulting from the movement of charged particles by an electric field, can be neglected due to the presence of buffer electrolyte in excess. Thus, in the employed setup, the flux is determined only by diffusion and convection. We will first derive the current from diffusional flux, then perturbations from convection will be considered.

For short times $t \ll t_\text{m}$ after the application of the working potential, the electrode behaves like a macroelectrode, i.e. planar diffusion towards the electrode surface is dominant. The time t_m is given as $\frac{\pi(d_\text{e}/2)^2}{16D} = 33.7\,\text{ms}$ [32]. Only within this regime of planar diffusion, the electrode is operated here. The condition is met by setting the electrode potential to zero for a sufficiently long time between two measurements and by generating the bubble when the diffusion layer has not yet fully developed. Accordingly, the flux to the electrode can be considered uniform and planar and a one-dimensional treatment is possible. Let z denote the coordinate perpendicular to the electrode surface (and the substrate), indicating the stand-off distance from the electrode surface. Then the chronoamperometric current I is given as [32]

$$I(t) = F A_\text{e} D \left.\frac{\partial c(z,t)}{\partial z}\right|_{z=0}, \tag{1}$$

where F is the Faraday constant (96485 C/mol), t the time, A_e the electrode area, and c the concentration of the electrolyte (Ru^{3+}-complex). Equation (1) connects mass conservation of the electrolyte and charge conservation of the electrode current via the Faraday constant.

Now the time evolution of the concentration profile is analyzed. After applying the working potential at $t = 0$, first a charging process occurs that largely stems from the formation of the molecular double layer at the electrode surface. This process, however, occurs so quickly that it can be neglected here [54]. After the charging process, the current is purely Faradaic and, as the electrolyte is reduced, a diffusion layer forms in vicinity to the electrode. This diffusion layer can be regarded as part of the wall shear rate sensor and must therefore be considered in more detail. Its formation is ruled by Fick's second law:

$$\frac{\partial c(z,t)}{\partial t} = D\frac{\partial^2 c(z,t)}{\partial z^2}. \tag{2}$$

For the present geometry, Eq. (2) can be solved analytically. When the working potential is applied at $t = 0$, the boundary conditions are $c(z{=}0,t) = 0$ and $c(z{>}0,t{=}0) = c_0$. The time-dependent formation of the concentration in the diffusion layer then follows as [32]

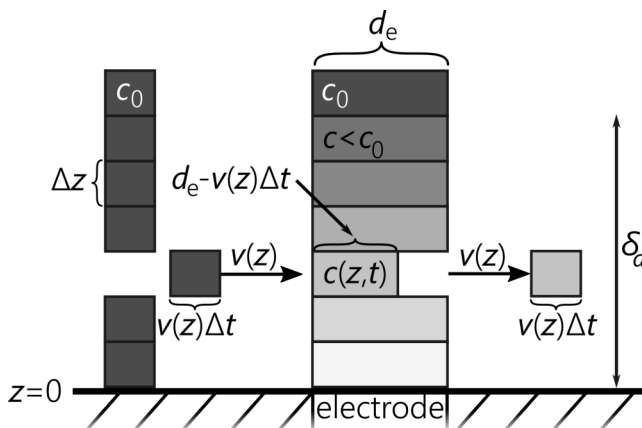$$c(z,t) = c_0 \,\text{erf}\left(\frac{z}{\sqrt{4Dt}}\right). \tag{3}$$

FIG. 2. Illustration of convection source term modeling. The squares to the left represent bulk liquid, the rectangles above the electrode characterize the diffusion layer.

A bubble oscillating in the liquid close to the electrode produces convection in the diffusion layer. This way a bubble affects the electrolyte concentration and generates an additional electrode current. For modelling the hydrodynamic perturbation, we assume that the convection within the diffusion layer is directed only parallel to the substrate surface. This assumption is justified because the diffusion layer thickness δ_d is very small ($\delta_d < d_e/2 = 12.5\,\mu$m for $t < t_M$, [55]). Figure 2 shows a schematic of the liquid displacement in the diffusion layer. For ease of description, the third spatial dimension is omitted. The bulk liquid has a concentration c_0 and is divided into small rectangles of height Δz. The convective flow moves liquid elements within a small period of time Δt from left to right, into the diffusion layer above the electrode. Each moving liquid element has a horizontal edge length $v(z)\Delta t$ (allowing for a velocity dependence on the vertical coordinate z). The diffusion layer itself is separated into rectangles of the same height (Δz) but with an edge length equaling the electrode diameter. When the rectangle of concentration c_0 moves from the bulk into the diffusion layer, it displaces a liquid rectangle of the same cross section and changes the concentration in the diffusion layer rectangle by $\Delta c = c(z,t+\Delta t) - c(z,t) = \frac{v(z,t)\Delta t}{d_e}c_0 - \frac{v(z,t)\Delta t}{d_e}c(z,t)$. The concentration change by convection during infinitesimally small time intervals $\Delta t \to 0$ is given by

$$\frac{\partial c(z,t)}{\partial t} = \frac{v(z,t)}{d_e}(c_0 - c(z,t)). \tag{4}$$

Combination of Eqs. (2) and (4) yields the total concentration change from diffusion and convection:

$$\frac{\partial c(z,t)}{\partial t} = D\frac{\partial^2 c(z,t)}{\partial z^2} + \frac{v(z,t)}{d_e}(c_0 - c(z,t)). \tag{5}$$

Thus, the above approach of modelling the electrode processes in only one dimension results in a relatively simple parabolic differential equation in which the convection appears as a velocity-dependent source term.

Appropriate boundary conditions for the electrolyte concentration in our setup are again $c(z{=}0,t) = 0$ (implicating an instantaneous reaction at the electrode surface) and $c(z{>}0,t{=}0) = c_0$ (homogenous bulk concentration).

To solve Eq. (5), a no-slip condition is imposed at the electrode surface and the velocity is linearized: $v(z,t) = v_0/d_e\, z$. This assumption is reasonable within the diffusion layer because the Schmidt number is very large ($Sc = \nu/D \cong 11000$, where ν is the kinematic viscosity of water), i.e., δ_d is much smaller than the hydrodynamic boundary layer δ_{hyd}. Note that the velocity profile

beyond the diffusion layer ($z > \delta_d \cong d_e/2$) has practically no effect on the concentration profile and consequently no effect on I because the concentration beyond the diffusion layer is already $\approx c_0$. Thus, Eq. (5) becomes

$$\frac{\partial c(z,t)}{\partial t} = D\frac{\partial^2 c(z,t)}{\partial z^2} + \frac{v_0(t)}{d_e^2}z\,(c_0 - c(z,t)). \tag{6}$$

The wall shear rate G is linked to $v_0(t)$ by

$$G(t) = v_0(t)/d_e. \tag{7}$$

By implementing Eq. (7), Eq. (6) can be rewritten as

$$\frac{\partial c(z,t)}{\partial t} = D\frac{\partial^2 c(z,t)}{\partial z^2} + G(t)\frac{z}{d_e}(c_0 - c(z,t)). \tag{8}$$

The wall shear stress σ of a flow with shear rate G is

$$\sigma(t) = \eta\,G(t). \tag{9}$$

Determination of G from a given electrode current $I(t)$ is an inverse problem. We solve it with an optimization approach for $G(t)$ using Eq. (8). To this end, the concentration profile $c(z,t)$ is simulated and perturbed trying several candidates of $G(t)$ until the resulting simulated current equals the measured current $I(t)$. Mathematically, the optimization rule reads

$$\min_{G(t)}\left[\text{abs}\left(I(t) - A_e F D \left.\frac{\partial c(z,t,G(t))}{\partial z}\right|_{z=0}\right)\right]. \tag{10}$$

In detail, the procedure for determination of $G(t)$ at subsequent time steps $t_0, t_1, t_2 \ldots t_j$ is as follows: An erf-profile is assumed as initial concentration profile at t_0 according to Eq. (3). The spatial concentration profile $c(z,t_1)$ at the next time step t_1 is calculated using Eq. (8) for several candidates of $G(t_1)$. The optimal candidate for $G(t_1)$ is found where, according to Eq. (1), the simulated current implied by the concentration profile resulting from the perturbation $G(t_1)$ equals the measured current $I(t_1)$: $\frac{\partial c(z,t_1,G(t_1))}{\partial z}|_{z=0} = I(t_1)/(FA_e D)$. The concentration profile that results from the optimal $G(t_1)$ is then used for calculation of $G(t_2)$. This procedure is applied for all subsequent time steps. It was found sufficient to simulate the diffusional-hydrodynamic boundary layer with a temporal resolution of $\frac{1}{10}T_S = 0.33\,\mu$s along a thickness of $10\,d_e$ in z-direction with a spatial resolution of 400 points, where the spatial mesh density of the discretization was set to decrease proportional to $1/z^2$. For the optimization and numerical solving of the differential equation a script in Matlab was developed. An example of the measured current together with the modelled current and the derived shear rates $G(t)$ are shown in the Appendix. Even with parallel computing, the rather expensive calculation takes about one day on a state of the art PC for one plane of wall shear rates.

In general, plasma generation and bubble dynamics are accompanied by free radicals and ions being generated that could be expected to cause an additional electric current and therefore to interfere with the measurement. However, any such influence on the measurement can be ruled out here. We could confirm this by applying a working potential below the reduction potential of the electrolyte. This way, Faradaic currents are turned off. Only residual currents and potentially spurious currents from radical and ion formation can be present. Under these conditions, we found that neither the plasma formation nor the bubble dynamics effect the measured current $I(t)$; i.e., no spurious currents were detected. Thus, radical or ion formation does not interfere with the measurements.

In summary, the steps of the entire procedure are as follows: (A) The chronoamperometric signals $I(t)$ from bubble collapse induced perturbations are measured spatially on a Cartesian grid. (B) The wall shear rates are retrieved from $I(t)$ by iterative optimizations and simulations of the respective concentration profiles. (C) The wall shear rates are numerically resampled on a radial grid (with the bubble center coinciding with the origin). This is possible as the wall shear rates are confirmed to show radial symmetry which in turn is a confirmation of a precise bubble generation.
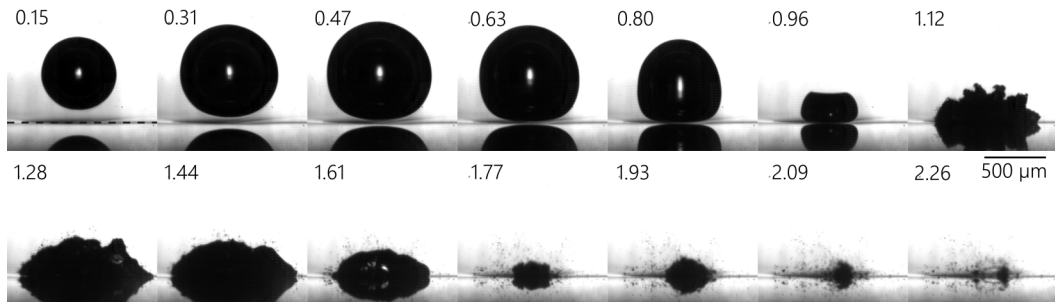
FIG. 3. Time series of a single bubble ($\gamma \cong 1$) collapsing at the substrate with the flush-mounted electrochemical sensor. The substrate extends horizontally at the bottom of the image (see the dashed line along the boundary in the first frame). The substrate surface can be also identified by the mirror image of the bubble at the bottom of the frames. Normalized times τ are given in the left top of each frame (the time of first collapse is $\tau = 1.00$ corresponding to $T_L = 88\,\mu$s). The (equivalent) bubble radius at maximum volume reaches a value of $R_{\max} = 425\,\mu$m (measured at $\tau = 0.47$).

III. RESULTS

A photographic series of the shape evolution of a single bubble that collapses at the substrate with the flush-mounted electrochemical sensor is presented in Fig. 3 in side view.

The same dynamics from a bottom view perspective through a transparent substrate is shown in Fig. 4. The time series is obtained in a similar experimental setup described in Ref. [56] without the electrochemical sensor that would not allow for a view through the substrate.

In both time series, the bubble is produced at $\tau = 0$. Initially, it is of spherical shape. It expands until $\tau \cong 0.5$. Then, the collapse phase begins. As the bubble shrinks, it translates toward the substrate whereby it is increasingly deformed. At the end of the collapse phase, a violent jet pierces the bubble in the axial direction (as described in Ref. [3] and references therein). Jetting becomes evident in Fig. 3 at $\tau = 0.96$ by the oblate shape and in Fig. 4 at $\tau = 0.93$ by the indentation at the axis of symmetry of the bubble. At $\tau = 0.98$ (Fig. 4) the jet is impacting on the substrate and has clearly pierced through the bubble. Consequently, the bubble takes a toroidal shape and finally collapses on the substrate to a ring shape at $\tau = 1.00$ (not shown).

After the jet has impacted, it flows radially outward, which increases the inner diameter of the bubble torus. The toroidally shaped bubble expands up to $\tau \cong 1.4$ with a "rugged" wall. Thereafter, the bubble begins to collapse for a second time. The respective collapse occurs around $\tau = 1.75$. Thus, the duration of the second oscillation is only about $0.75\,T_L$, mainly as a result from energy losses during the first collapse. After the second collapse, the bubble has largely disintegrated, and
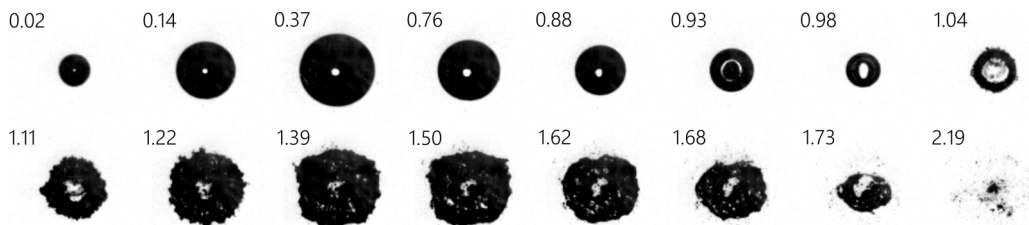

FIG. 4. Time series of a single bubble that collapses in vicinity to a substrate as in Fig. 3, but now imaged in bottom view through a transparent substrate ($R_{\max} = 475\,\mu$m, $T_L = 97.5\,\mu$s). Normalized times τ are indicated in the top left corner of each frame.

many small bubbles remain. Only in the center, one larger bubble is formed. It undergoes some afterbounces (see Fig. 3, $\tau \geqslant 1.77$, and Fig. 4, $\tau = 2.19$).

The corresponding evolution of the wall shear rates is presented in Fig. 5 (read the figure from left to right and top to bottom).

The first two frames show the effect of the essentially radial bubble oscillation (volume pulsation) before the first collapse. Right below the bubble on the substrate, a small liquid layer stagnates. Consequently, around the axis of symmetry wall shear rates are low. At intermediate distances from the axis of symmetry, the near-wall liquid layer follows the bubble oscillation. Still, shear rates only reach up to 2.3 $\times 10^5 \, \text{s}^{-1}$ (at $\tau = 0.36$). For larger distances they decrease for geometric reasons.

We would like to draw particular attention to the frames at $\tau = 0.95 \ldots 1.17$. They reflect the interaction of the (axial) jet with the substrate. The jet impacts around $\tau = 0.95$ on the substrate and subsequently spreads annularly outwards. Around the axis of symmetry, a marked stagnation area is present, which appears as a "crater" of low shear rates. The axial jet is expected to have an about sigmoidal shape when it pierces the bubble [10,14]. Consequently, while the jet tip already spreads over the substrate starting from the axis of symmetry, more abaxial parts of the jet impact onto the substrate later. Therefore, the jet-substrate interaction intensifies until $\tau = 1.11$. Wall shear rates are now about 20 times higher than during the initial radial oscillations (they reach up to $4.2 \times 10^6 \, \text{s}^{-1}$).

Starting at $\tau = 1.11$, and more clearly visible from $\tau = 1.15$ onwards, high shear rates on the outer side of the bubble torus are produced by the rebounding bubble. The rebound takes part directly at the boundary and produces, therefore, significant wall shear rates ($3.1 \times 10^6 \, \text{s}^{-1}$). During the rebound process, they are exerted on a ring that expands radially because the involved flows spread radially outward.

From around $\tau = 1.42$, an annular flow of opposite direction builds up. It runs inward, toward the axis of symmetry. Its formation and dynamics are best perceived in Video A of the Supplemental Material, which shows the entire time series of the wall shear rates [57]. This flow arises from the shrinking of the torus that starts from its outer side (see Figs. 3 and 4). The flow pushes the outer wall of the toroidal bubble inward. This inward-directed, annular flow generates the highest shear rates on a large geometrical extent on the surface. As it converges towards the axis of symmetry, it further intensifies for geometric reasons. Thus, for many applications this flow may be considered the most significant one.

At the same time, an outward directed annular flow still persists at the inner side of the torus bubble. Both flows collide between $\tau = 1.54$ and 1.66. The radial flow running towards the axis of symmetry seems to outweigh the opposite flow and the torus radius continues to shrink from the outer side (compare also to Fig. 4, $\tau = 1.73$).

During the collision of both flows, high stagnation pressures must build up along the ring where the collision takes place. By this event, shear rates suddenly decrease, apparently due to dissipation, splashing, and flow detachment from the substrate. Therefore, the second collapse, which occurs shortly after, is not anymore associated with high wall shear rates.

After the second collapse, there are no significant shear rates exerted by the bubble-induced flows. Nevertheless, in a confined region at the axis of symmetry, higher shear rates are still detected. They appear at $\tau = 1.66$ and $\tau = 2.26$ at the center and result from a small bubble that is formed as secondary cavitation at the axis of symmetry by the shock wave that is emitted during the collapse of the toroidal bubble. We frequently see this small, secondary cavitation bubble in our bubble imaging series. It shows its own dynamics with some afterbounces and probably jetting, too. Correspondingly, the associated wall shear rates pulsate (see Video A of the Supplemental Material [57]).

Further insight into the processes at the substrate surface can be obtained from energy considerations. A rough estimation of the energy stored in the bubble from volume work against the ambient pressure of $p_0 = 100 \, \text{kPa}$ yields: $E_b = \frac{4}{3} \pi R_{\text{max}}^3 \, p_0 = 38 \, \mu\text{J}$. The kinetic energy in the near-wall liquid layer can be calculated from the measured wall shear rates. We assume a linear velocity profile for calculating the kinetic energy E_{kin} of the near-wall liquid layer of thickness $d_e/2$, which is in the order of the diffusion layer thickness. The time-dependent kinetic energy within the liquid layer of the entire measurement plane is then given by
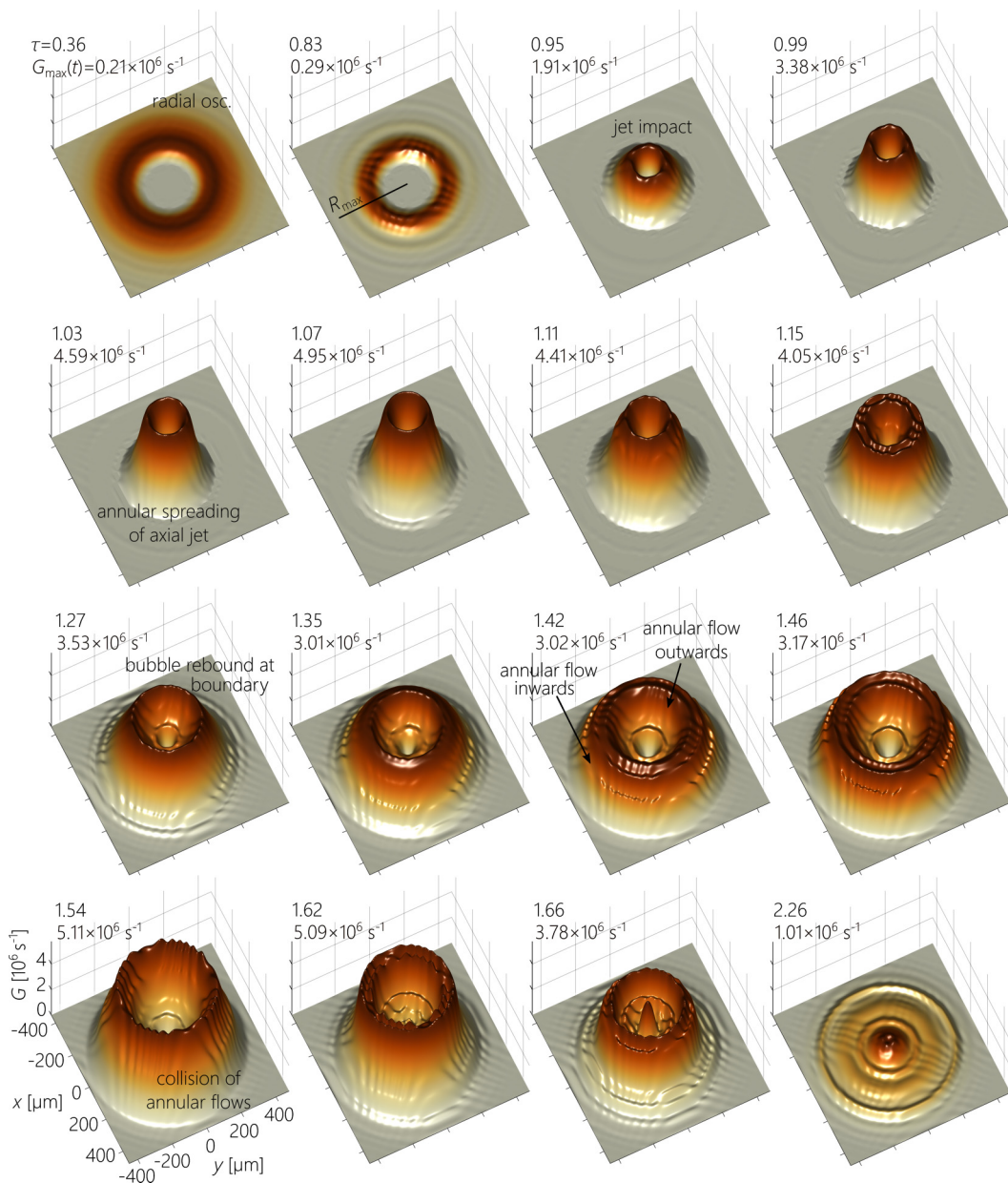
FIG. 5. Electrochemical wall shear microscopy of a single bubble collapsing in the vicinity of a rigid boundary ($R_{max} = 425\,\mu$m; $\gamma \cong 1$). Wall shear rates are height-coded over the substrate that extends in the x/y plane. To present the entire time evolution in one figure, we use the same height scale for all frames but adjust the color scale to each frame individually. The respective values of the maximum wall shear rates (corresponding to the darkest colors in each frame) are indicated in the second row of the top left corner of each frame (the brightest coding always corresponds to $0\,$s^{-1}). Normalized times are given in the upper row of each top left corner of each frame. The bubble is generated at $\tau = 0$; the time series presentation starts at $\tau = 0.36\,(= 32\,\mu$s) and ends at $\tau = 2.26\,(= 200\,\mu$s). Note the different time intervals between the frames. The corresponding time series of the bubble shape is presented in Figs. 3 and 4. For comparison, R_{max} is depicted (see the second frame); note that the initial contact radius is much smaller than R_{max}. For the dynamics of the entire time series at high resolution, see Video A of the Supplemental Material [57].
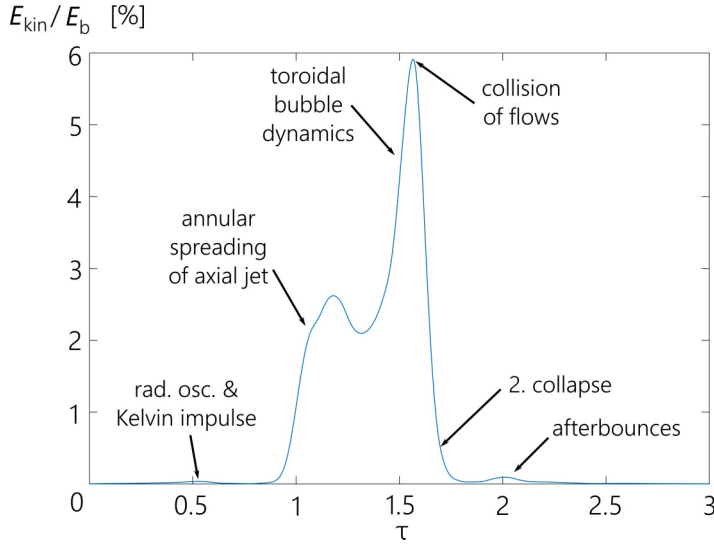
FIG. 6. Kinetic energy in the near-wall liquid layer in percentage of the initial bubble energy.

$E_{\text{kin}}(t) = \frac{1}{2}\rho \int_{-450\,\mu\text{m}}^{450\,\mu\text{m}} \int_{-450\,\mu\text{m}}^{450\,\mu\text{m}} \int_{0}^{d_e/2} (G(x,y,t) \times z)^2 \, dz \, dx \, dy$, where $\rho = 1000\,\text{kg/m}^3$ is the mass density of water. In Fig. 6, the kinetic energy associated with the near-wall layer is given in percent of the total initial bubble energy.

It can be seen that (for $\gamma \cong 1$) the bubble dynamics concentrates up to 6 % of the potential energy of the expanded bubble into the liquid flow directly at the boundary. This concentration occurs during the toroidal bubble dynamics that takes part directly at the substrate during the phase, when a strong flow towards the axis of symmetry is generated (see $\tau = 1.46$ in Fig. 5). In comparison, the axial jet from the first collapse is associated with only about half of that kinetic energy in the near-wall liquid layer. Interestingly, the second collapse is characterized by very little liquid-substrate interaction, due to the flow collision that had occurred before.

Some further details also become visible in the energy representation. When the bubble starts its first collapse phase ($\tau \cong 0.5$) it moves toward the boundary, a behavior that can be predicted from the preservation of the Kelvin impulse (see Refs. [16,19,58]). Due to the bubble migration, liquid between bubble and substrate is displaced (in Fig. 3 the distance between bubble and substrate shrinks between $\tau = 0.31$ and $\tau = 0.80$). This displacement is reflected by a small rise in the kinetic energy of the near-wall layer. Furthermore, at the end of the time series, some afterbounces from the small bubble remaining after the second collapse in the center become apparent.

The spatial distribution of the maximum wall shear rate experienced at any time during the entire bubble dynamics of Fig. 5 is shown in Fig. 7 color and height coded. In the central area ($x, y \leqslant 350\,\mu\text{m}$) high shear rates are reached (between $2 \times 10^6\,\text{s}^{-1}$ and $6 \times 10^6\,\text{s}^{-1}$). Within this area, two rings of highest wall shear rates stand out. Their origin can be explained by the time series of Fig. 5. The inner ring ($x = 100\,\mu\text{m}$) results from the axial jet that pierced the bubble. The outer ring is produced by the annular jet toward the axis of symmetry, just before the collision of flows.

Significant wall shear rates are observed up to a distance of $x = 400\,\mu\text{m}$, which is in the order of the maximum bubble radius ($R_{\text{max}} = 425\,\mu\text{m}$). Toward larger distances, the wall shear rates decline fast.

We conclude this analysis with Fig. 8, showing the dimensionless times of *when* the maximum wall shear rates of Fig. 8 are reached, as a function of x and y. The substrate surface is divided into four regions: A, B, C, D, where the maximum wall shear rate in A occurs first and in D latest. The peripheral region A experiences only low wall shear rates. They are produced by volume pulsation and motion of the bubble toward the substrate before the first collapse. The region B experiences
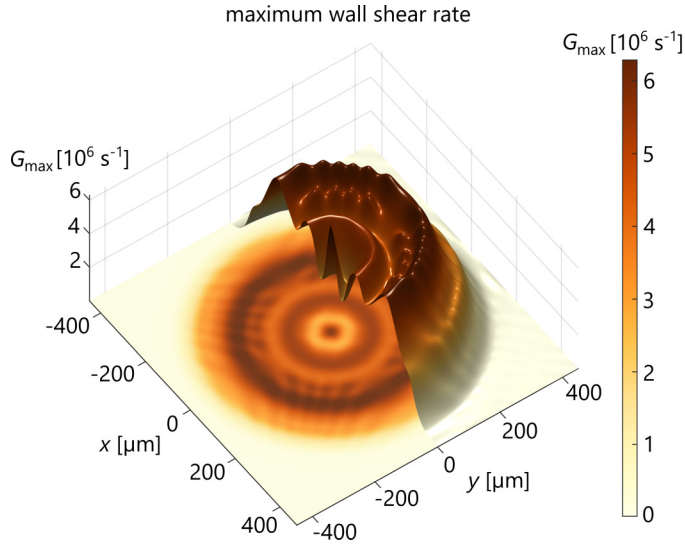
FIG. 7. Maximum wall shear rate $G_{max}(x,y) = \max_t[G(x,y,t)]$ occurring during the bubble collapse in the measured region. The values are shown both height coded and in planar projection.

its highest wall shear rates by the axial jet after it has pierced the bubble during the first collapse. The highest wall shear rates in region C are generated by the annular jet flow towards the axis of symmetry which is produced by the toroidal bubble collapse (the second collapse). Note that the coding of region C gets darker toward the axis of symmetry (meaning that the peak shear rate
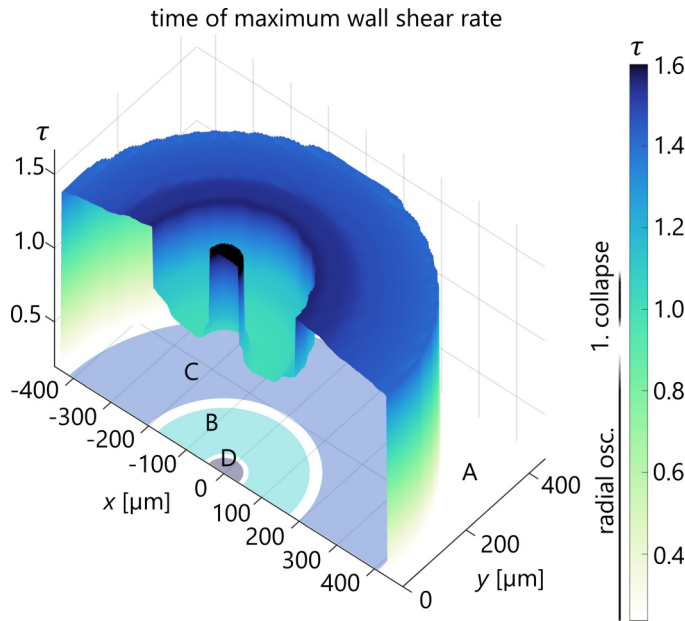

FIG. 8. Time of occurrence of maximum wall shear rate. The substrate surface can be divided into four sections, A–D (according to the time of maximum wall shear rate). The τ scale is clipped at 1.6 for best contrast.

occurs later). This indicates the flow is directed towards the center. This annular flow is stopped at $x \approx 200\,\mu$m where it collides with the outward directed jet flow. The fourth region, D, where the maximum shear stress occurs latest, is not directly caused by the collapse dynamics. It covers just a small area around the axis of symmetry where the largest remnant bubble shows its own dynamics after the main bubble has disintegrated.

IV. DISCUSSION

A wall shear rate microscope using a microelectrode that is flush mounted into a test substrate has been presented. The microelectrode was used to carry out high-speed chronoamperometric measurements on a mass-transfer-limited reaction process that was accelerated by the convection of the flow under study—here a collapsing bubble. Therefrom, the wall shear rates have been derived by a one-dimensional model that couples diffusion and convection within the diffusion layer.

The method has been designed to analyze cavitation events that involve the generation of highly unsteady flows of enormous velocities and gradients directly at substrate surfaces. Other available experimental tools, especially those that rely on the determination of the velocity field or velocity profile to deduce the shear rates, are not sufficient as they lack the necessary spatial and often also temporal resolution. Additionally, the calculation of gradients from measurement data is not ideal as it is prone to random noise. Noise is largest for the measurement of *wall* shear rates because the velocity gradients are typically highest at the wall. Moreover, the conduction of measurements is impaired by geometric conditions that restrict the placement of sensors, tracers, and the optical accessibility. The electrochemical method employed here avoids these problems. It measures directly in the boundary layer and can easily handle high shear rates which even improve the signal-to-noise ratio because the sensor signal is proportional to $\frac{dc}{dz}\big|_{z=0}$.

Use of a *micro*electrode provides a fast response time and high spatial resolution. Geometrically, the electrode is a microelectrode, however, diffusion-wise, it is operated as a *macro*electrode. That means that the diffusional flux to the electrode is planar which is achieved here by operating it only in short measurement intervals. This allows for model simplifications and a one-dimensional modelling.

To resolve the wall shear rates spatially, single bubbles of the same properties are repeatedly produced at precisely adjusted locations by means of a laser pulse. The resulting flows are spatially scanned with the electrode by measuring at shifted locations with respect to the bubble center. The synchronized high-speed imaging captures details of bubble oscillation, collapse and jet formation, rebound, and subsequent toroidal bubble dynamics. Correlation of the images with the time-resolved wall shear rates reveal quantitative and qualitative details of the flows induced by the bubble collapse at the solid substrate.

Significant wall shear rates occur in a circular area with a radius in the order of the maximum bubble radius. This explains why circular cleaning regions with radii similar to the radii of active bubbles are observed in single bubble cleaning experiments [18] and in ultrasonic cleaning [22]. Within the circular area, shear rates are of similar magnitude. The area, however, can be divided into distinct regions that are affected at different stages of the bubble dynamics and with different flow directions.

For many applications, the maximum wall shear rate experienced at the substrate surface is important. For example, the values reported for cell deformation, permeabilization and lysis by Marmottant *et al.* [59] range from $10^3\,\text{s}^{-1}$ (cell wall stretching) to $10^5\,\text{s}^{-1}$ (wall rupture). The maximum shear rates measured here are well above $10^6\,\text{s}^{-1}$ and thus lead to the expectation of definite rupture of cell walls adjacent to a violently collapsing bubble of the investigated size. This is in accordance to the experiments reported by Wolfrum *et al.* [60] and Dijking, Ohl, and collaborators [26,27,61]. Cell wall stretching is expected at distances from the axis of symmetry that are larger than $0.95\,R_{\max}$. Removal of surface-attached micro- and nanoparticles by oscillating bubbles for damage-free cleaning [18,62,63] requires sufficiently high but also well controlled shear rates directly at a solid substrate. Numerical estimates of required shear values for sliding and rolling of attached spheres of 100 nm radius lead to values in the range of $10^6\,\text{s}^{-1}$ and beyond [64]. The knowledge of the produced shear rates, and the feasibility to precisely and repeatedly produce single
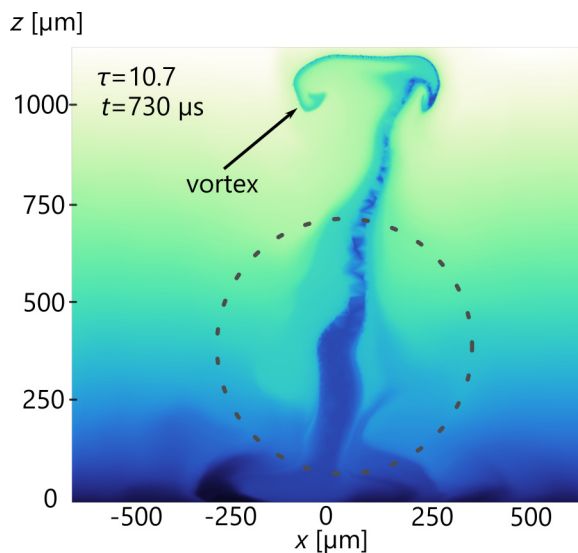
FIG. 9. Lagrangian ink map of a collapsing bubble, illustrating the liquid displacement a long time after the collision of flows (at $\tau = 10.7$). Perspective as in Fig. 3 with the boundary extending horizontally at $z = 0$. The circle indicates the bubble shape at maximum expansion. Liquid from the boundary layer (dark blue) is ejected and colliding flows have detached and formed a ring vortex. Experimental data obtained by particle imaging velocimetry; for details, see Ref. [56].

bubbles by a laser pulse, renders the investigated collapsing bubbles interesting as controlled shear sources for surface manipulations or microfluidic applications.

The wall shear rate microscope now resolves the axial jet impact on the substrate, the subsequent annular spreading of the jet flow, and the collision of flows produced by the toroidal bubble dynamics. The importance of these flows for surface cleaning has been pointed out previously [18]. The jet impact is characterized by high wall shear rates and the development of a marked stagnation area around the axis of symmetry.

During collapse and rebound, the bubble assumes a toroidal shape. The highest wall shear rates are reached during the second bubble oscillation when the outer torus wall moves toward the axis of symmetry.

The complex bubble dynamics leads to a situation in which outward and inward directed annular flows collide, which provokes a sudden decrease of wall shear rates. After the collision of flows, no further significant interaction between bubble induced flows and substrate is observed. To understand the reasons, and relate it to applications, the entire flow field in the space above the substrate surface must be considered. In Fig. 9, the flow field is shown long after the collision of flows ($\tau \cong 11$). It is obtained with a different measurement method (particle image velocimetry), adapted from Reuter *et al.* 2017 [56]. The flow field is presented here by a Lagrangian ink map, integrated over time, which effectively shows the liquid displacement. One clearly sees that liquid from the near-wall layer (dark blue) is ejected into the bulk. The pattern arises from a ring vortex that has formed during collision of flows. It detaches from the substrate and migrates into the bulk ("free vortex," see Ref. [56]).

Thus, the high stagnation pressures produced during the collision of flows result in flow separation and lift-off from the boundary. This marks the end of significant flow substrate interaction. In surface cleaning, the detached flow can lift particles into the overlying bulk of liquid.

V. CONCLUSION

The extreme conditions produced by cavitation bubbles inspire an ongoing progress in experimental techniques. In particular, interaction of cavitation with substrates challenges the experimenter.

This interaction is intense but short-lived. Yet it is of great practical importance. For example, in the widespread application of ultrasonic cleaning, flows are generally required to exceed a certain wall shear threshold to achieve detachment of surface adhered contamination. But at the same time, shear forces have to stay below material damage thresholds. This way, a process window for ultrasonic cleaning is defined. While the process window is often known from the material side, the wall shear forces exerted by collapsing bubbles need to be determined.

We have constructed a high-speed wall shear rate microscope for spatiotemporal measurement of rapid and transient wall shear flows. It relies on fast electrochemical signal recordings and has been used to study locations and time evolution of the shear rates at a solid boundary during the collapse of an adjacent single cavitation bubble. Synchronized high-speed imaging allows us to relate the shear rates to the bubble dynamics. This way, the wall shear rates produced by a single collapsing cavitation bubble were resolved directly at the surface of a solid substrate in high spatial and temporal resolution. Local flow field features that extend on scales smaller than 50 μm could be resolved. The data also enabled the assessment of surface stresses from the wall shear stresses for the latter of which values of up to $6.2 \, \text{kN} \, \text{m}^{-2}$ have been found.

Furthermore, fundamental details about bubble-generated flows were revealed and consistently related to the respective stages of bubble dynamics. Shear rates arising from the impact and spreading of the bubble-piercing jet that is produced along with bubble collapse were resolved in time and space. Several flow reversals on the surface were observed, in particular, the collision of annular flows upon the collapse of the toroidal bubble. For the parameters investigated, the highest wall shear rates occur when the toroidal bubble touches the surface and its dynamics take place directly at the surface, right before the collision of flows.

From the experimental data provided here, together with results from the flow field measurements and simulations, a complete picture on the physical interactions caused by cavitation bubbles on solids is emerging. Furthermore, with the knowledge of the generated wall shear forces, precisely produced single bubbles can serve as well controlled actuators for wall shear in microfluidic applications.

Future implementations of electrochemical wall shear rate microscopy might reveal more on the interaction of cavitation bubbles and solid surfaces at other stand-off distances γ. Moreover, the technique might be applied to other unsteady, reproducible microscopic flow phenomena at solid surfaces, like the impact of drops or jets on liquid films. In addition, a similar model and procedure may be applicable with hot-wire anemometers integrated into a solid substrate, so that instead of our electrochemical diffusion layer a thermal boundary layer would be exploited.

APPENDIX

For illustration of the procedure of derivation of the wall shear rates from the chronoamperometric data, in Fig. 10 raw data is presented for a measurement position that is located around 300 μm from the axis of symmetry: The measured current density is shown together with the simulated one (left). The respective shear rates used for the simulation are shown on the right.

The agreement is striking so that the modeled current almost entirely matches the measured one. Only around $t \cong 100 \, \mu \text{s}$, there is a short period of about 10 μs in which the current decreases faster
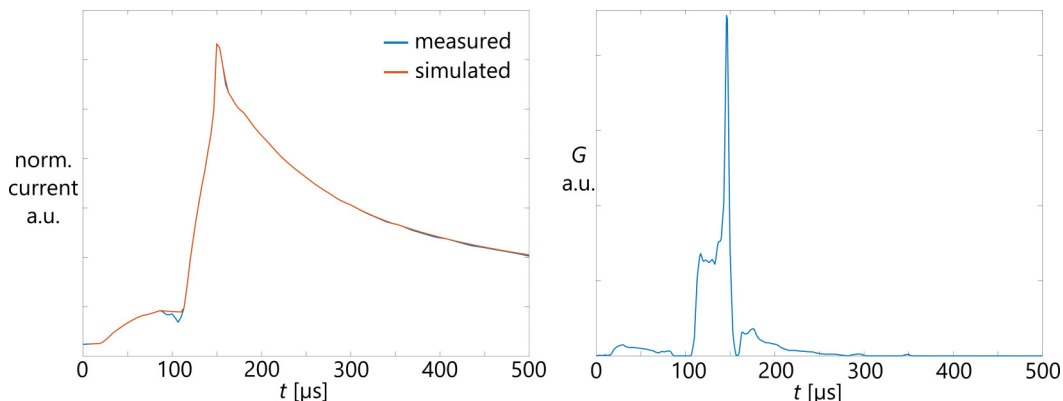
FIG. 10. Left: Comparison between measured current density at the electrode and simulated one during the convection event produced by the cavitation bubble. Right: Respective calculated shear rates.

than it can be modeled. Possible reasons are that the liquid film width decreases to a width smaller than the diffusion layer, or that a laminar flow transiently reverses, bringing back already reacted (reduced) electrolyte. Both situations are not included in the model, while for all other times, the matching is nearly perfect.

---

[1] T. G. Leighton, *The Acoustic Bubble* (Academic Press, San Diego, 1994).

[2] C. E. Brennen, *Cavitation and Bubble Dynamics* (Oxford University Press, Oxford, 1995).

[3] W. Lauterborn and T. Kurz, Physics of bubble oscillations, Rep. Prog. Phys. **73**, 106501 (2010).

[4] C. F. Naudeé and A. T. Ellis, On the mechanism of cavitation damage by nonhemispherical cavities collapsing in contact with a solid boundary, J. Basic Eng. **83**, 648 (1961).

[5] N. D. Shutler and R. B. Mesler, A photographic study of the dynamics and damage capabilities of bubbles collapsing near solid boundaries, J. Basic Eng. **87**, 511 (1965).

[6] M. S. Plesset and R. B. Chapman, Collapse of an initially spherical vapor cavity in the neighborhood of a solid boundary, J. Fluid Mech. **47**, 283 (1971).

[7] W. Lauterborn and H. Bolle, Experimental investigations of cavitation-bubble collapse in the neighborhood of a solid boundary, J. Fluid Mech. **72**, 391 (1975).

[8] A. Shima, K. Takayama, Y. Tomita, and N. Ohsawa, Mechanism of impact pressure generation from spark-generated bubble collapse near a wall, AIAA J. **21**, 55 (1983).

[9] O. Lindau and W. Lauterborn, Cinematographic observation of the collapse and rebound of a laser-produced cavitation bubble near a wall, J. Fluid Mech. **479**, 327 (2003).

[10] A. Pearson, J. R. Blake, and S. R. Otto, Jets in bubbles, J. Eng. Math. **48**, 391 (2004).

[11] Y. Tomita and A. Shima, Mechanisms of impulsive pressure generation and damage pit formation by bubble collapse, J. Fluid Mech. **169**, 535 (1986).

[12] A. Vogel, W. Lauterborn, and R. Timm, Optical and acoustic investigations of the dynamics of laser-produced cavitation bubbles near a solid boundary, J. Fluid Mech. **206**, 299 (1989).

[13] T. S. Lundgren and N. N. Mansour, Vortex ring bubbles, J. Fluid Mech. **224**, 177 (1991).

[14] J. P. Best, The formation of toroidal bubbles upon the collapse of transient cavities, J. Fluid Mech. **251**, 79 (1993).

[15] A. Philipp and W. Lauterborn, Cavitation erosion by single laser-produced bubbles, J. Fluid Mech. **361**, 75 (1998).

[16] E. A. Brujan, G. S. Keen, A. Vogel, and J. R. Blake, The final stage of the collapse of a cavitation bubble close to a rigid boundary, Phys. Fluids **14**, 85 (2002).

[17] Q. X. Wang, K. S. Yeo, B. C. Khoo, and K. Y. Lam, Vortex ring modelling of toroidal bubbles, Theor. Comput. Fluid Dyn. **19**, 303 (2005).

[18] F. Reuter and R. Mettin, Mechanisms of single bubble cleaning, Ultrason. Sonochem. **29**, 550 (2016).

[19] J. R. Blake, The Kelvin impulse: Application to cavitation bubble dynamics, J. Austral. Math. Soc. Ser. B **30**, 127 (1988).

[20] D. F. Rivas and B. Verhaagen (eds.), Special issue: Cleaning with bubbles, Ultrason. Sonochem. **29**, 517–628 (2016).

[21] N. S. M. Yusof, B. Babgi, Y. Alghamdi, M. Aksu, J. Madhavan, and M. Ashokkumar, Physical and chemical effects of acoustic cavitation in selected ultrasonic cleaning applications, Ultrason. Sonochem. **29**, 568 (2016).

[22] F. Reuter, S. Lauterborn, R. Mettin, and W. Lauterborn, Membrane cleaning with ultrasonically driven bubbles, Ultrason. Sonochem. **37**, 542 (2017).

[23] M. R. Bailey, V. A. Khokhlova, O. A. Sapozhnikov, S. G. Kargl, and L. A. Crum, Physical mechanisms of the therapeutic effect of ultrasound (a review), Acoust. Phys. **49**, 369 (2003).

[24] M. Wan, Y. Feng, and G. ter Haar, Eds., *Cavitation in Biomedicine* (Springer Netherlands, Dordrecht, 2015).

[25] D. L. Miller, S. V. Pislaru, and J. F. Greenleaf, Sonoporation: Mechanical DNA delivery by ultrasonic cavitation, Somat. Cell Mol. Genet. **27**, 115 (2002).

[26] R. Dijkink *et al.*, Controlled cavitation–cell interaction: Trans-membrane transport and viability studies, Phys. Med. Biol. **53**, 375 (2006).

[27] C.-D. Ohl *et al.*, Sonoporation from jetting cavitation bubbles, Biophys. J. **91**, 4285 (2006).

[28] K. R. Rau, P. A. Quinto-Su, A. N. Hellman, and V. Venugopalan, Pulsed laser microbeam-induced cell lysis: Time-resolved imaging and analysis of hydrodynamic effects, Biophys. J. **91**, 317 (2006).

[29] K. Ferrara, R. Pollard, and M. Borden, Ultrasound microbubble contrast agents: Fundamentals and application to gene and drug delivery, Annu. Rev. Biomed. Eng **9**, 415 (2007).

[30] J. L. Compton, A. N. Hellman, and V. Venugopalan, Hydrodynamic determinants of cell necrosis and molecular delivery produced by pulsed laser microbeam irradiation of adherent cells, Biophys. J. **105**, 2221 (2013).

[31] J. L. Compton, J. C. Luo, H. Ma, E. Botvinick, and V. Venugopalan, High-throughput optical screening of cellular mechanotransduction, Nat. Photonics **8**, 710 (2014).

[32] J. Wang, *Analytical Electrochemistry*, 3rd ed. (Wiley-VCH, Weinheim, 2006).

[33] V. G. Levich, *Physicochemical Hydrodynamics*, 2nd ed. (Prentice-Hall, New York, 1962).

[34] J. E. Mitchell and T. J. Hanratty, A study of turbulence at a wall using an electrochemical wall shear-stress meter, J. Fluid Mech. **26**, 199 (1966).

[35] R. J. Goldstein, Ed., *Fluid Mechanics Measurements* (Hemisphere Publishing, Washington, DC, 1983).

[36] H. B. Hanekamp, P. Bos, and R. W. Frei, Electrochemical detectors in flowing liquid systems: An assessment of their use, Trends Anal. Chem. **1**, 135 (1982).

[37] E. Kjeang, B. Roesch, J. McKechnie, D. A. Harrington, N. Djilali, and D. Sinton, Integrated electrochemical velocimetry for microfluidic devices, Microfluid. Nanofluidics **3**, 403 (2007).

[38] H. D. Dewald and B. A. Peterson, Ultrasonic hydrodynamic modulation voltammetry, Anal. Chem. **62**, 779 (1990).

[39] C. Hagan and L. A. Coury, Comparison of hydrodynamic voltammetry implemented by sonication to a rotating disk electrode, Anal. Chem. **66**, 399 (1994).

[40] J. Klima, C. Bernard, and C. Degrand, Sonoelectrochemistry: Transient cavitation in acetonitrile in the neighbourhood of a polarized electrode, J. Electroanal. Chem. **399**, 147 (1995).

[41] P. R. Birkin and S. Silva-Martinez, A study of the effect of ultrasound on mass transport to a microelectrode, J. Electroanal. Chem. **416**, 127 (1996).

[42] E. Maisonhaute, C. Prado, P. C. White, and R. G. Compton, Surface acoustic cavitation understood via nanosecond electrochemistry. Part III: Shear stress in ultrasonic cleaning, Ultrason. Sonochem. **9**, 297 (2002).

[43] E. Maisonhaute, B. A. Brookes, and R. G. Compton, Surface acoustic cavitation understood via nanosecond electrochemistry. 2. The motion of acoustic bubbles, J. Phys. Chem. B **106**, 3166 (2002).

[44] C. E. Banks and R. G. Compton, Voltammetric exploration and applications of ultrasonic cavitation, Chem. Phys. Chem. **4**, 169 (2003).

[45] B. G. Pollet, J.-Y. Hihn, M.-L. Doche, J. P. Lorimer, A. Mandroyan, and T. J. Mason, Transport limited currents close to an ultrasonic horn, J. Electrochem. Soc. **154**, E131 (2007).

[46] J.-Y. Hihn, M.-L. Doche, A. Mandroyan, L. Hallez, and B. G. Pollet, Respective contribution of cavitation and convective flow to local stirring in sonoreactors, Ultrason. Sonochem. **18**, 881 (2011).

[47] B. G. Pollet, *Power Ultrasound in Electrochemistry: From Versatile Laboratory Tool to Engineering Solution* (Wiley-VCH, 2012).

[48] P. R. Birkin, H.-M. Hirsimäki, J. G. Frey, and T. G. Leighton, Mass transfer enhancement produced by laser induced cavitation, Electrochem. Commun. **8**, 1603 (2006).

[49] F. Reuter, C. Cairós, and R. Mettin, Vortex dynamics of collapsing bubbles: Impact on the boundary layer measured by chronoamperometry, Ultrason. Sonochem. **33**, 170 (2016).

[50] A. Vogel and W. Lauterborn, Acoustic transient generation by laser-produced cavitation bubbles near solid boundaries, J. Acoust. Soc. Am. **84**, 719 (1988).

[51] F. Marken, J. C. Eklund, and R. G. Compton, Voltammetry in the presence of ultrasound: Can ultrasound modify heterogeneous electron transfer kinetics? J. Electroanal. Chem. **395**, 335 (1995).

[52] G. R. Hood and J. C. Williams, The viscosity and fluidity of aqueous potassium ferrocyanide solutions, Ohio J. Sci. **35**, 415 (1935).

[53] M. Muzikář and W. R. Fawcett, Medium effects for very fast electron transfer reactions at electrodes: The [Ru(NH3)6]3+/2+ system in water, J. Phys. Chem. B **110**, 2710 (2006).

[54] E. Maisonhaute, P. C. White, and R. G. Compton, Surface acoustic cavitation understood via nanosecond electrochemistry, J. Phys. Chem. B **105**, 12087 (2001).

[55] C. Amatore and E. Maisonhaute, When voltammetry reaches nanoseconds, Anal. Chem. **77**, 303 A (2005).

[56] F. Reuter, S. R. Gonzalez-Avila, R. Mettin, and C.-D. Ohl, Flow fields and vortex dynamics of bubbles collapsing near a solid boundary, Phys. Rev. Fluids **2**, 64202 (2017).

[57] See Supplemental Material at http://link.aps.org/supplemental/10.1103/PhysRevFluids.3.063601 for Video A, which shows a complete time series of the dynamics of the wall shear rates produced by one collapsing bubble.

[58] J. R. Blake, D. M. Leppinen, and Q. Wang, Cavitation and bubble dynamics: The Kelvin impulse and its applications, Interface Focus **5**, 20150017 (2015).

[59] P. Marmottant and S. Hilgenfeldt, Controlled vesicle deformation and lysis by single oscillating bubbles, Nature **423**, 153 (2003).

[60] B. Wolfrum, R. Mettin, T. Kurz, and W. Lauterborn, Observations of pressure-wave-excited contrast agent bubbles in the vicinity of cells, Appl. Phys. Lett. **81**, 5060 (2002).

[61] R. Dijkink and C.-D. Ohl, Measurement of cavitation induced wall shear stress, Appl. Phys. Lett. **93**, 254107 (2008).

[62] W. Kim, T.-H. Kim, J. Choi, and H.-Y. Kim, Mechanism of particle removal by megasonic waves, Appl. Phys. Lett. **94**, 81908 (2009).

[63] A. Thiemann, T. Nowak, R. Mettin, F. Holsteyns, and A. Lippert, Characterization of an acoustic cavitation bubble structure at 230 kHz, Ultrason. Sonochem. **18**, 595 (2011).

[64] H. F. Okorn-Schmidt *et al.*, Particle cleaning technologies to meet advanced semiconductor device process requirements, ECS J. Solid State Sci. Technol. **3**, N3069 (2013).